By G.S. Bhat and
Harindra J.S. Fernando

Remotely Driven Anomalous Sea-Air Heat Flux

Over the North Indian Ocean During the Summer Monsoon Season

Photo credit: San Nguyen

> Physical processes underlying the South Asian summer monsoon are complex. The seasonally persistent winds over surrounding seas and precipitation over land embody the quintessential characteristics of the summer monsoon—not to mention its splendor, which has long aroused the curiosity of scientists and artists alike.

ABSTRACT. The atmosphere typically receives heat from the open tropical ocean; an exception is the western and central Arabian Sea during the summer monsoon season. This article analyzes in situ observations from buoys and ships and examines mechanisms responsible for the reverse sea-air interfacial heat flux that have yet to be addressed. Key factors are the horizontal advection of heat and the heat flux derived via mixing and entrainment of air from above the atmospheric mixed layer in a Richardson number regime where shear-driven mixing would not normally be expected. This study invites a fresh look at the physics of entrainment and mixing in the atmospheric boundary layer. The reverse heat flux observations offer an opportunity to test the efficacy of physics encapsulated in boundary layer parameterization schemes for coupled models.

INTRODUCTION

For most inhabitants of Southeast Asia, monsoon season means bountiful rainfall, although for ancient Arab traders, it meant a seasonally reversing wind system over the North Indian Ocean that had remarkable bearing on sailing. Physical processes underlying the South Asian summer monsoon are complex (e.g., Webster et al., 1998; Gadgil, 2003). The seasonally persistent winds over surrounding seas and precipitation over land embody the quintessential characteristics of the summer monsoon—not to mention its splendor, which has long aroused the curiosity of scientists and artists alike. Monsoonal winds collect water vapor from south of the equator in the Indian Ocean, from the Arabian Sea, and from the Bay of Bengal and transport it to Southeast Asia (Figure 1). The highest rates of evaporation over the tropical ocean during the peak monsoon months of July and August are observed between

10°S and 20°S in the Indian Ocean sector slightly to the north of the Mascarene high (Figure 1a). Secondary peaks are observed over the central Arabian Sea and the southern Bay of Bengal, which happen to be regions with the highest evaporation rates in the Northern Hemisphere. The strong surface winds involved in monsoon circulation (Figure 1b) are known to be partly responsible for this evaporation, because the evaporation rate is proportional to the surface wind speed (e.g., Liu et al., 1979; Zeng et al., 1998). We would expect the corresponding surface sensible heat flux (Q_s) also to be high in this region. However, data reveal that this is not the case. Q_s can be either negligible or even negative over the western and central Arabian Sea (Figure 1c). The flow of heat from water to air is the norm over the open ocean in the tropics (Figure 1c), consistent with the notion that the ocean first absorbs solar radiation and then the atmosphere receives part of it. A negative

Q_s means the atmosphere supplies heat to the ocean when the temperature of the air (T_a) exceeds that of the water below. The geographic location of the Arabian Sea and its mean wind directions are such that hot air blows from the land toward the sea near its western boundary (Figure 1b). There, T_a can exceed sea surface temperature (SST), resulting in a negative Q_s (e.g., Red Sea, Gulf of Oman, and the east coast of Oman; Figure 1c). Figure 1b shows that the mean wind direction is almost parallel to the east coast of African, and, therefore, direct land effects on surface air temperature are at best limited to nearshore areas in the western Arabian Sea.

The present study addresses the physical mechanisms responsible for the anomalous behavior of Q_s over the interior of the Arabian Sea during July and August. Horizontal advection of heat becomes important when SST varies spatially. If, for some reason, the SST of an area is less compared to its surroundings, then advection brings in air that can be warmer than the local SST. Near the African east coast, ocean dynamics produces a large pool of cold water. Here, strong, persistent surface winds blow parallel to the coast and drive oceanic Ekman transport to the right of the wind direction, which causes intense upwelling of cold water. In fact, the area exhibiting the largest negative Q_s in Figure 1c is the upwelling

region of the Somali current (Schott et al., 2009). We expect the upwelling effect to decay with increasing distance from the coast. In reality, this is not the case, and upwelling effects are felt several hundred kilometers from the African coast. Mesoscale eddies or filaments of cold water that form near the Omani coast travel to the central Arabian Sea, creating pockets of cold SSTs (e.g., Fischer et al., 2002). Cold filaments are highly transient in nature, and horizontal gradients in SST attributed to them vary widely in space and time (e.g., Fischer et al., 2002). It is not clear if cold eddies can maintain negative Q_s on monthly and longer time scales over a broader area away from the coast. Therefore, apart from cold water filaments and horizontal advection, we need to look for other atmospheric processes capable of supporting the negative

Q_s that may be active over the Arabian Sea during the summer monsoon season.

In what follows, we demonstrate that the anomalous behavior of Q_s can arise from turbulent entrainment at the top of the atmospheric boundary layer (ABL). This occurs in a range of gradient Richardson numbers above 0.25 but less than 1 (i.e., in a regime where shear-driven mixing is not normally expected). The geographic location of the Arabian Sea, surrounded by deserts to its west and north, and the presence of strong low-level monsoonal winds render this process possible.

DATA AND METHODS
Data

We use global surface air temperature, dew point temperature (T_d), SST, and wind velocity data from the ERA-Interim

reanalysis (Dee et al., 2011) monthly average products at 1° × 1° horizontal resolution. Q_s and latent heat flux (Q_L) are estimated using the bulk method (Zeng et al., 1998), considering wind-speed-dependent exchange coefficients for heat fluxes (Appendix A). Woods Hole Oceanographic Institution (WHOI) operated a moored buoy at 61.5°E, 15.5°N in the Arabian Sea for a year, starting in October 1994 (Weller et al., 1998), and WHOI has been operating one in the northern Bay of Bengal at 18°N, 89°E since December 2014. Data from both these buoys are used. RAMA (Research Moored Array for African-Asian-Australian Monsoon Analysis and Prediction) buoys have been deployed in the Indian Ocean since 2007 (McPhaden et al., 2009). Their data, used here, are made available by the TAO (Tropical Atmosphere Ocean)
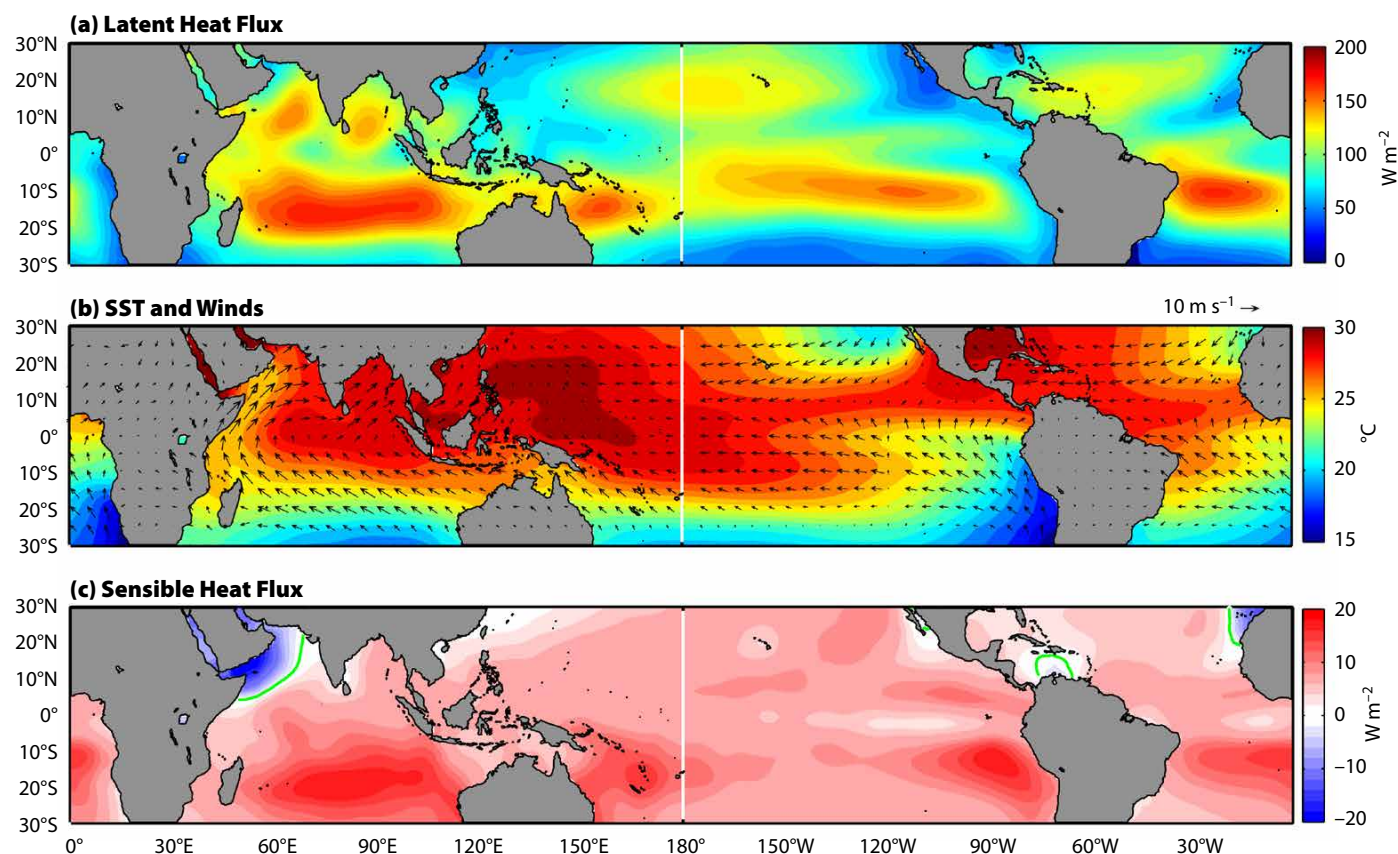

FIGURE 1. (a) Spatial distribution of the sea-air latent heat flux over the tropical ocean. Latent heat flux is directly proportional to evaporation rate. The fluxes were calculated using the bulk method (e.g., Liu et al., 1979) with a wind-speed-dependent exchange coefficient (Supplementary Figure S1). (b) Sea surface temperature (SST, color shaded) and wind vector (arrows). The length of the arrow at the top right corner of the panel shows the magnitude of the wind vector. (c) Spatial distribution of the sea-air sensible heat flux. Green lines indicate zero values of sensible heat flux, and heat flows from the atmosphere into the ocean in areas shown in blue. The figure is based on 10 years of ERA-Interim (1995–2004) monthly data for July and August.

project office of the US National Oceanic and Atmospheric Administration/Pacific Marine Environmental Laboratory. Buoy data analyzed here are the daily average values (daily averages are computed when higher temporal resolution data are available). Surface and upper-air data were collected over the eastern Arabian Sea from the Indian ORV *Sagar Kanya* from June to August 2002 under the Arabian Sea Monsoon Experiment (ARMEX) program (e.g., Rao, 2005). The ship surveyed around 16.9°N, 71.2°E from June 25 to July 10, 2002 (Bhat, 2005). Observations were made over the southern and central Bay of Bengal from August 22 to September 8, 2014, from the same ship, as part of the Ocean Mixing and Monsoon (OMM) program (Lucas et al., 2014; Wijesekera et al., in press), and are also used in the study.

Theory

Temperature evolution is governed by the energy equation, and our analysis is primarily based on energy conservation applied to a suitably chosen atmospheric layer of finite thickness (Figure 2). The control volume (CV) includes the surface layer and the mixed layer (ML) part of the ABL (Figure 2). There are four fluxes across the CV boundary: Q_s (exchanged across the sea-air interface), Q_a (horizontal advection), R_{net} (net radiation), and Q_t (heat flux at the top surface of the CV). Heat flowing into the CV is taken as positive. If heat storage within the CV is neglected, then (in the absence of phase change of water)

$$Q_s + R_{net} + Q_a + Q_t = 0. \qquad (1)$$

Q_s is parameterized by the equation (e.g., Liu et al., 1979)

$$Q_s = \rho\, C_p\, C_h\, U_s\, \Delta T, \qquad (2)$$

where ρ and C_p are the density and specific heat of air at constant pressure, respectively, C_h is the exchange coefficient for heat (e.g., Appendix A), U_s is the surface wind speed (normally at 10 m above sea level), and $\Delta T = (SST - T_a)$. All terms on the right-hand side of Equation 1 are positive except for ΔT. Hence, Q_s gets its sign from ΔT. Combining Equations 1 and 2 gives an equation governing ΔT:

$$\Delta T = -\frac{R_{net} + Q_a + Q_t}{\rho\, C_p\, C_h\, U_s}, \qquad (3)$$

with Q_a given by

$$Q_a = -\rho\, C_p\, U\, \partial T_a / \partial s, \qquad (4)$$

where s is the distance measured along the mean air flow trajectory. R_{net} is the sum of absorption in the spectrum's shortwave regime and emission in the longwave regime. Daily average R_{net} is always negative and its magnitude, when expressed in equivalent ABL cooling rate, is 1°C–3°C day^{-1} (e.g., Dopplick, 1979). Note that Q_t is always positive, and its magnitude depends on the presence or absence of turbulent entrainment in the layer capping the atmospheric ML.

RESULTS

Values shown in Figure 1 are based on monthly reanalysis data products averaged for 10 seasons. Although very useful for getting a global view, they do not provide insights into the temporal evolution of ΔT within a monsoon season. Figure 3 shows time series of daily SST, T_a, U_s, and wind direction at two locations, one in the Arabian Sea and the other in the Bay of Bengal. At the Arabian Sea buoy location, $SST \geq T_a$ (i.e., $\Delta T \geq 0$) until the first week of June (Figure 3a), and their difference is reduced thereafter, coinciding with the beginning of the summer monsoon season, which is characterized by strong winds. During late July and in August, $SST < T_a$ (i.e., $\Delta T < 0$), and the change of the sign of ΔT to positive in September coincided with a decrease in U_s. Figure 3a shows that ΔT fluctuates on very short time scales as well. When
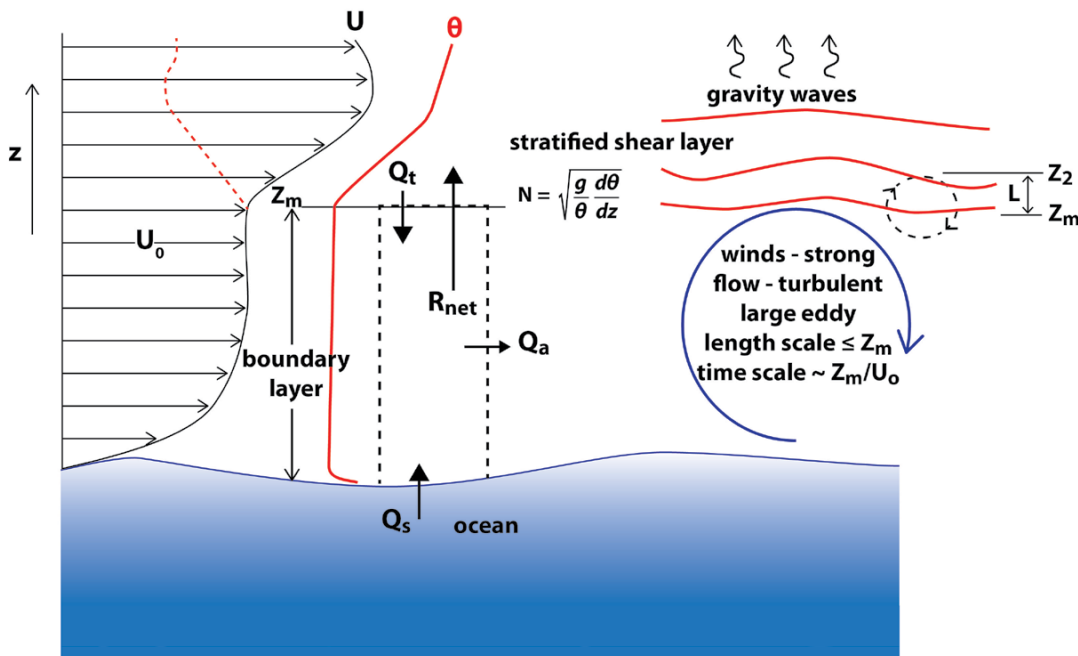

FIGURE 2. A schematic of some important physical processes taking place in the lower troposphere. The dashed lines mark the boundaries of the control volume considered for the energy balance. Its lower boundary (not seen) is just above the water surface. A constant value of potential temperature θ (red line) means air is well mixed, and the layer of the atmosphere with a constant θ is the mixed layer. Here, the flow is turbulent. Part of the atmosphere where θ increases with height is stably stratified, and any perturbation here generates gravity waves. Changing wind speed (U) with height gives wind shear. Typically, the base of fair weather cumulus clouds is located just above the mixed layer in the tropics.

ΔT transitioned between positive and negative values from June to September, the wind direction (Figure 3c) remained southwesterly and showed little variation. Figure 3b shows the time series of SST, T_a, and U_s at 12°N, 90°E measured by sensors on the RAMA buoy. Here, T_a remains below SST most of the time; however, the difference between the two is often very small, and T_a even exceeded SST on a few occasions, albeit marginally. Note that the instances of large dips in T_a are normally associated with rain showers.

Figure 3 also demonstrates that wind speeds were high when $\Delta T < 0$. To further understand the connection between wind speed and ΔT, the Figure 4 scatter plot includes all available buoy data in the Indian Ocean within 20° latitude from the equator. For clarity, data measured over the Arabian Sea (Figure 4a), the Bay of Bengal (Figure 4b, including data from RAMA buoys north of 5°N and the WHOI Bay of Bengal buoy), and the Indian Ocean (Figure 4c, RAMA buoys between 5°N and 16°S) are plotted separately. Certain trends are seen in Figure 4 despite large scatter. Over the Arabian Sea and the Bay of Bengal, (Figure 4a,b), ΔT tends to decrease with wind speed, which is consistent with Equation 3. For wind speeds of more than 6 m s^{-1}, ΔT became negative on many days over the Arabian Sea, and its lowest values of less than -1.5°C occurred for wind speed around 10 m s^{-1}, followed by an increasing trend with the wind speed. Similar behavior is observed over the Bay of Bengal, but the lowest value of ΔT is ~ -1°C, and negative ΔT occurs for wind speeds above 3 m s^{-1}. Negative ΔT is also observed over the equatorial Indian Ocean (Figure 4c); however, its decreasing trend with the wind speed is not that prominent. Here, low values of ΔT occur in the 4–7 m s^{-1} range, and ΔT shows an increasing trend with wind speed above 10 m s^{-1}.

Q_L is a measure of the rate of evaporation and is parameterized by an equation of the form (e.g., Liu et al., 1979)

$$Q_L = \rho \, L_v \, C_e \, U_s \, \Delta q, \qquad (5)$$

where L_v is the latent heat of vaporization of liquid water, C_e is the exchange coefficient for vapor (e.g., Zeng et al., 1998; Appendix A), and $\Delta q = (q_s - q_a)$, with q being the specific humidity and the subscripts s and a referring to the sea surface (assumed to be saturated at SST and multiplied by 0.98 to account for seawater salinity; e.g., Fairall et al., 1996) and air, respectively. The variation of Δq with wind speed is shown in Figure 4d–f. At the Arabian Sea WHOI buoy location, Δq decreases with U_s, declines to almost zero around 10 m s^{-1}, and then increases, closely analogous to the trends shown by ΔT. Over the Bay of Bengal, Δq decreases with U_s, reaches a minimum around 8 m s^{-1}, and the minimum value remains above 1.5 gm kg^{-1}. A minor dependence of Δq on wind speed is observed over the equatorial Indian Ocean (Figure 4f).

The product $U_s \cdot \Delta q$ (evaporation parameter, EP, hereafter) matters for evaporation. To understand the connection between the occurrence of negative ΔT and EP, scatter plots of these parameters are shown in Figure 4g–i (since the number of data points are several thousand in Figure 4h and 4i, values of EP in these plots are shown when $U_s > 5$ m s^{-1}, as the main interest here is negative ΔT at high wind speeds). At the Arabian Sea buoy location, EP increases with ΔT. Buoy data show that relative humidity was ~90% when ΔT was minimum here (Weller et al., 1998). Since SST was low, q_s, which is a function of SST, was also less, and Δq values were close to zero, which is reflected in the small value of EP. The highest EP occurred during winter. Over the Bay of Bengal (Figure 4h), the minimum EP occurs in the vicinity of $\Delta T \sim 0$°C in the north bay (WHOI
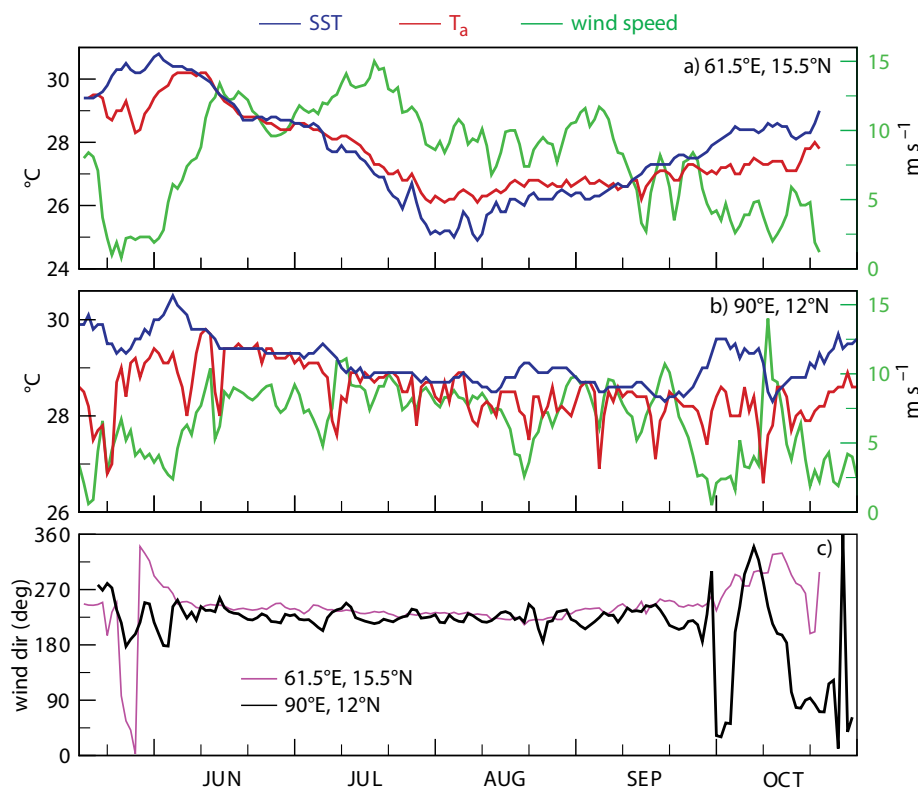

FIGURE 3. (a) Sea surface temperature (SST), air temperature (T_a), and wind speed measured with a Woods Hole Oceanographic Institution (WHOI) buoy in the Arabian Sea in 1995. (b) Same as (a) but in the Bay of Bengal with a Research Moored Array for African-Asian-Australian Monsoon Analysis and Prediction (RAMA) buoy in 2014. (c) Wind direction measured by the buoys during the corresponding periods. The meteorological convention for wind direction is used (i.e., a wind direction of 270° means a westerly wind). All variables shown are daily average values.

buoy location), whereas the minimum values are observed between −0.3°C and 2°C in the central and southern bay (RAMA buoys). EP increases as ΔT becomes more negative. Over the equatorial Indian Ocean (Figure 4i), except for a few odd data points, EP increases with increasing ΔT for ΔT >1°C.

DISCUSSION

Equation 3 governs ΔT, and the sign of ΔT is decided by the sum of all three terms in the numerator: net radiative cooling, horizontal advection of heat, and heat flux at the top of the ML. When the sign of a term is negative, it drives ΔT toward positive. Let us examine the signs of the terms in Equation 3 at the Arabian Sea WHOI buoy location for the July to August 1995 period. The ABL cools through emission of longwave radiation, and R_{net} is always negative (e.g., ~ −12 W m^{-2} for an ABL height of 500 m at a cooling rate of 2°C day^{-1}; see, e.g., Dopplick, 1979). Therefore, only Q_a and/or Q_t could have produced a negative ΔT.

Since surface air is in continuous contact and interacts with water below, we expect T_a and SST fields to be similar on daily and longer time scales. Then the second term (Q_a) depends on SST and wind fields. Surface wind was consistently southwesterly (Figure 3c). Figure 1b shows that air trajectories are either parallel to the lines of constant SST or from a region of lower to warmer SST. Then, $\partial T_a/\partial s$ is either zero or positive, and Equation 4 yields a zero or negative Q_a. The mean climatology (e.g., Figure 1b) does not reveal the actual SST field of a given year or changes that occur on intraseasonal and on shorter time scales. In particular, mesoscale eddies make the instantaneous SST field complicated over the central Arabian Sea during the summer monsoon season. The SST field underwent large changes in the vicinity of the buoy from June to August 1995 (Fischer et al., 2002), affecting the temperature gradient in Equation 4, hence the horizontal heat advection term. During June and July, SSTs to the southwest of the buoy (seen in

Figure 12a–c in Fischer et al., 2002) were warmer, and Q_a >0. During early August (i.e., a time period having the largest negative ΔT), the SST gradient along the wind direction was very weak if not marginally positive to the southwest of the buoy (seen in Figure 12e in Fischer et al. (2002). Thus, the heat flux due to horizontal advection was positive, nearly zero, and negative, and Q_a could have made ΔT negative during certain time periods but not throughout July and August.

An estimation of Q_t is obtained from Equation 1. Q_s was in the −5 to −18 W m^{-2} range during late July and early August (Weller et al., 1998). As noted earlier, we may take R_{net} ~ −12 W m^{-2}. Neglecting the horizontal advection, Q_t required

to maintain a steady state is more than 15 W m^{-2} and can be as high as 30 W m^{-2}, which is large considering that the average Q_s is ~10 W m^{-2} (Figure 1c). What could be the source of such a large Q_t? Q_t becomes significant if turbulent entrainment and mixing are present at the CV's top surface (Figure 2). The atmosphere above the ML is stably stratified in density (i.e., it requires work to mix the air from above with the ML air). In meteorology, it is common to relate the stratification of the atmosphere to the vertical gradient of potential temperature θ, defined as $\theta = T(1,000/p)^\kappa$, where T and p are temperature and pressure of air at height z, and $\kappa = 0.284$. p is expressed in hecto Pascal (hPa) units, and θ in K. When
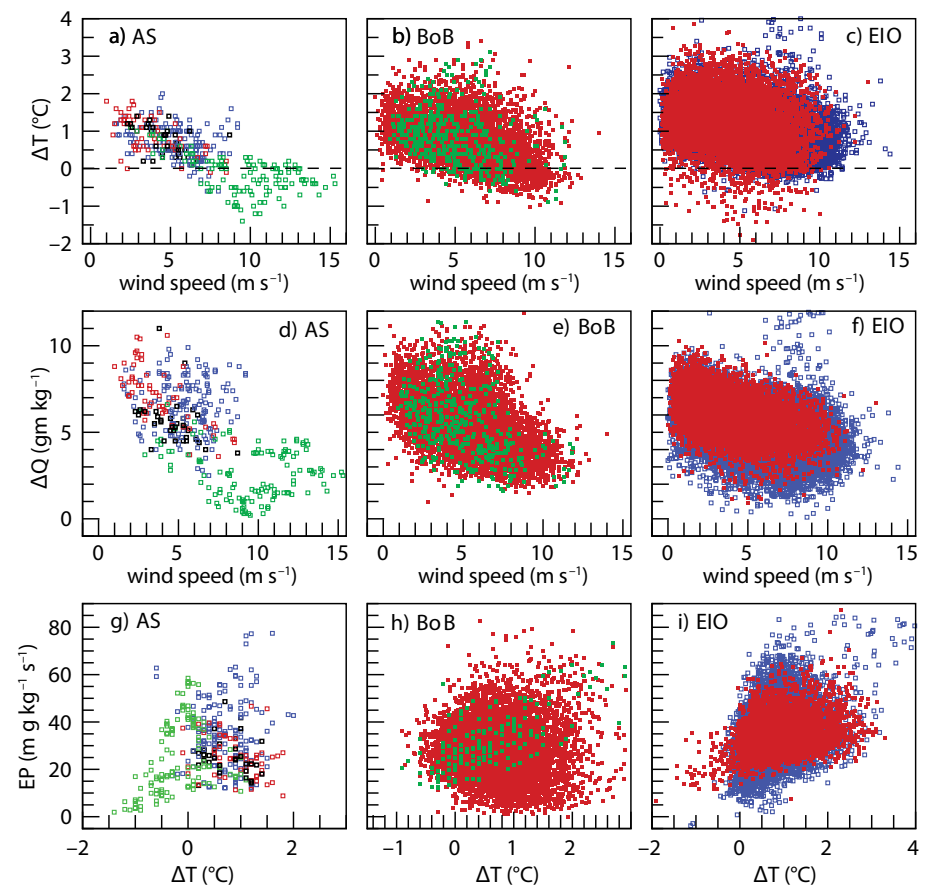

FIGURE 4. (a–c). Scatter plots of wind speed and sea-air temperature difference ΔT. (d–f) Scatter plots of wind speed and sea-air humidity difference ΔQ. (g–i) Scatter plots of sea air temperature difference and evaporation parameter (EP). Plots are based on daily average values, using available buoy data in the Indian Ocean and not limited to the summer monsoon season. AS = Arabian Sea (WHOI buoy). BoB = Bay of Bengal north of 5°N (green symbols = WHOI buoy, red symbols = RAMA buoys). EIO = Equatorial Indian Ocean (RAMA buoys = red symbols, 5°S to 5°N; blue symbols = 5°S to 16°S). Different colors of symbols in panels a, d, and g correspond to different seasons: October = black; November to March = blue, April and May = red, and June to September = green.

θ increases with height, atmosphere is stably stratified. Wind shear could be present (Figure 2). When density stratification and wind shear coexist (i.e., stratified shear layer, SSL), Kelvin-Helmoltz instability is possible and is governed by the gradient Richardson number Ri_g given by (Drazin and Howard, 1966):

$$Ri_g = \frac{g}{\theta}(\partial\theta/\partial z)/(\partial U/\partial z)^2, \qquad (6)$$

where g is the acceleration due to gravity, U the wind speed, and z the height (Figure 2). Ri_g characterizes the role of wind shear in destabilizing a stably stratified flow. Linear stability analysis (Miles and Howard, 1964) and energy arguments (Miles, 1986), respectively, yield 0.25 and unity for the value of critical Ri_g below which instabilities and hence turbulent mixing may appear. In both theories, energy for destabilization comes from within the SSL.

Flow in the ABL (Figure 2) differs from canonical stably stratified flows in two respects. First, turbulent eddies of various sizes occur in the ML. A part of the kinetic energy needed to destabilize the flow in the SSL comes from energetic eddies impinging from below. Second, internal wave radiation may carry energy upward from the SSL (Figure 2). A stability analysis of the SSL with external energy addition/removal is not available nor is a theoretical criterion based on a critical Ri_g. This very configuration, however, has been studied in the laboratory by Strang and Fernando (2001a), whose findings on critical Ri_g have been shown to be consistent with the field results (Strang and Fernando, 2001b). Different types of instabilities have been observed depending on Ri_g, with strong mixing at the interface occurring for $Ri_g \leq 1$ and the entrainment rate decreasing by an order of magnitude for higher Ri_g, eventually approaching molecular values (Strang and Fernando, 2001a).

Next, we examine if $Ri_g \leq 1$ occurs in the North Indian Ocean during the summer monsoon season by analyzing the surface and upper air data collected during ARMEX and OMM cruises (Figures 5 and 6). (Upper air data are not available at the WHOI buoy location in the Arabian Sea.) Figure 5a shows that T_a > SST (i.e., $\Delta T < 0$) prevailed the majority of the time from June 26 to July 6 in the Arabian Sea, while the opposite was the case in the Bay of Bengal (Figure 5b). Figure 6 shows four representative cases (denoted by S1, S2, S3, and S4 in Figure 5) of the vertical profiles of virtual potential temperature (θ_v, the potential temperature corrected for water vapor's effect on air density) and wind speed in the lowest 2.5 km of the atmosphere. On June 26 (S1), strong wind shear extended across the top of the mixed layer, whereas on July 9 (S2), the wind shear was relatively weak. Ri_g is calculated considering a 100 m thick atmospheric layer starting from 150 m above the surface (Figure 6c). It is observed that $Ri_g < 1$ for the June 26 sounding in a layer that is more than 200 m deep capping the ML (Figure 6c; i.e., turbulent entrainment and mixing is possible based
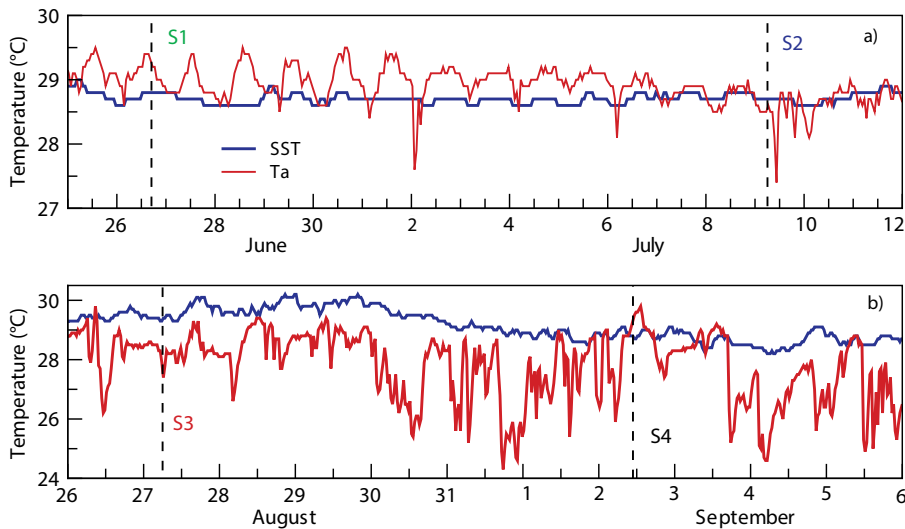

FIGURE 5. (a) SST and air temperature measured over the Arabian Sea near 16.9°N and 71.2°E over the Arabian Sea in 2002 from the Indian ORV *Sagar Kanya*. (b) Same as (a) but measured during the Ocean Mixing and Monsoon cruise in 2014. Data shown are 30-minute average values. Line color code is the same in both plots. Dashed vertical lines show radiosonde launch times, and their corresponding profiles are shown in Figure 6. The line colors in Figure 6 correspond to those of S1, S2, S3, and S4 in this figure.
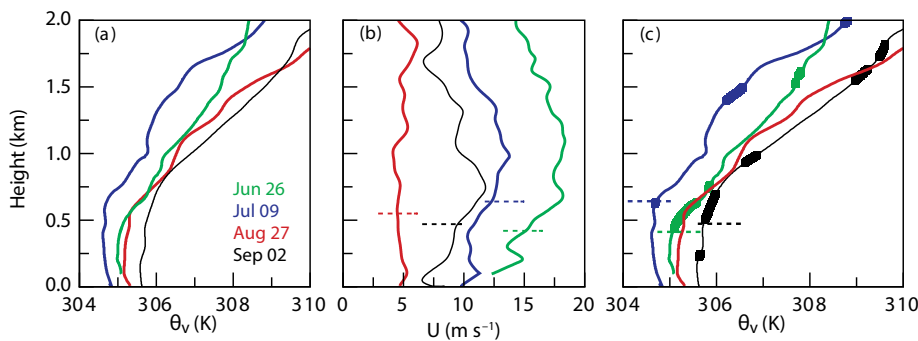

FIGURE 6. (a) Vertical profiles of virtual potential temperature based on the radiosonde data collected during research cruises in the Arabian Sea and the Bay of Bengal. See Figure 5 for the times of radiosonde launches. (b) Vertical profiles of horizontal wind. (c) Vertical profiles of virtual potential temperature. Layers where the gradient Richardson number is less than unity are shown by solid symbols. Dashed horizontal lines in (b) and (c) indicate the top of the mixed layer.

on Strang and Fernando, 2001b). For the July 9 sounding, instability is present near the top of the ML, but the unstable layer does not extend into the stable layer. For the August 27 sounding (S3), wind shear is weak and $Ri_g > 1$; hence, no instability. For the September 2 sounding (S4), Ri_g is <1 in a thick layer above the ML, and hydrodynamic instability and turbulent entrainment is possible. At the time of this sounding, T_a was rapidly increasing, then exceeded SST and remained warmer than SST for the next several hours (Figure 5b).

The question is: What could be the magnitude of Q_t? To get a feel for the Q_t, we consider one specific example—the formulation of Q_t used in the Geophysical Fluid Dynamics Laboratory (GFDL) coupled climate model (Lock et al., 2000; Anderson et al., 2004)—and estimate its predicted Q_t for the ARMEX soundings shown in Figure 6. Details of the calculation are given in Appendix B, and the results are shown in Table 1. The estimated Q_t for June 26 and July 9 conditions are 42 W m^{-2} and 14 W m^{-2}, respectively. The corresponding required values of Q_t from the ML energy balances are 20 W m^{-2} and 7 W m^{-2}, respectively. Thus, the conditions over the Arabian Sea are capable of yielding a significant Q_t. The estimated Q_t is nearly twice that required, and further studies are needed to narrow down the gap between these two.

The unique geographic location of the Arabian Sea provides an ideal setting for hydrodynamic instability to operate. A strong, low-level, cross-equatorial jet, known as the Somali jet or Findlater jet, is present over the western Indian Ocean near the east coast of Africa every summer (Findlater, 1969). This jet turns into the Arabian Sea around 10°N, and moves over the central Arabian Sea and toward the Indian subcontinent (Findlater, 1969). The core of the jet is 1–1.5 km above the surface, and strong wind shear is associated with it. Over the Arabian Sea, dry and warm air of desert origin overlies cool and moist marine air, and a

low-level temperature inversion is present during the summer monsoon season (Ghosh, 1978). The inversion base is a few hundred meters above the surface near the African coast, it slowly lifts to more than a kilometer eastward of 65°E (Ghosh, 1978), and the inversion extends all the way to the east coast of India on some occasions (Bhat, 2005). Thus, in the vicinity of the top of the atmospheric ML, both stable stratification and strong wind shear are present over the Arabian Sea, creating favorable conditions for hydrodynamic instability to manifest.

CONCLUDING REMARKS

Over the central Arabian Sea, two factors can produce a negative sea-air temperature difference: (1) horizontal advection of heat flux in the atmospheric boundary layer that can be attributed to ocean dynamics and oceanic mesoscale eddies, and (2) strong surface winds and/or hydrodynamic instability of a stably stratified shear layer above the atmospheric mixed layer. The imperceptible interplay between turbulent entrainment at the top of the mixed layer and ΔT near the surface is a consequence of energy conservation of the atmospheric boundary layer. The resulting magnitude of Q_t is small compared to the latent heat flux, but Q_t can be large compared to the average sea-air sensible heat flux over the tropical ocean. ΔT influences fluxes at the sea-air interface through stability of the surface layer (e.g., Zeng et al., 1998). Furthermore, water vapor concentration normally decreases with height above the mixed layer. Turbulent entrainment here and mixing of the drier air with the air

below reduces the water vapor concentration in the entire atmospheric boundary layer. This helps maintain the sea-air water vapor difference and hence the surface evaporation. The observed increase of EP in Figure 4 as ΔT goes more negative (except at the Arabian Sea buoy location, the reasons for which are yet to be understood) supports such a possibility. Thus, entrainment at the top of the ML not only controls Q_s but can impact the hydrological cycle as well (Holtslag and Boville, 1993). Therefore, understanding and parameterization of physical processes associated with entrainment at the top of the mixed layer are crucial for coupled models.

Relative contributions of remote and local influences on the rate of entrainment are yet to be measured and quantified over the open ocean. A combination of laboratory models and targeted field campaigns covering a range of atmospheric conditions are needed. Note that most of the relevant past field campaigns over the ocean have focused on developing algorithms for surface fluxes based on local variables, but we assert that relevant physical processes can be present in the air layer from 0.5 km to 1 km above the surface, necessitating nonlocal flux parameterizations. Incorporation of such nonlocal processes is essential for producing realistic Q_t and hence air-sea fluxes in predictive models. An important inference from Figure 6 is that the shear layer is thin for cases with $Ri_g < 1$. Good vertical resolution, better than 100 m at the top of the mixed layer, is required in coupled models to predict realistic values of Q_t. ⓒ

TABLE 1. Q_t needed from the surface energy balance (Equation 1) and Q_t estimated from the Geophysical Fluid Dynamics Laboratory (GFDL) atmospheric boundary layer parameterization scheme for two cases of atmospheric conditions that prevailed over the Arabian Sea on June 26 and July 9, 2002. See Figures 5 and 6 for more details.

Profile	Q_t Estimated (W m^{-2})	Q_t Needed (W m^{-2})
June 26, 2002	42	20
July 9, 2002	14	7

REFERENCES

Anderson, J.L., V. Balaji, A.J. Broccoli, W.F. Cooke, T.L. Delworth, K.W. Dixon, L.J. Donner, K.A. Dunne, S.M. Freidenreich, S.T. Garner, and others. 2004. The New GFDL Global Atmosphere and Land Model AM2–LM2: Evaluation with prescribed SST simulations. *Journal of Climate* 17:4,641–4,673, http://dx.doi.org/10.1175/JCLI-3223.1.

Bhat, G.S. 2005. Convection inhibition energy of the inversion and the suppressed rainfall over the Arabian Sea during July 2002. *Mausam* (ARMEX Special Issue) 56:89–96.

Bhat, G.S., S. Gadgil, P.V. Harish Kumar, S.R. Kalsi, P. Madhusoodanan, V.S.N. Murty, C.V.K. Prasada Rao, V. Ramesh Babu, L.V.G. Rao, R.R. Rao, and others. 2001. BOBMEX: The Bay of Bengal Monsoon Experiment. *Bulletin of the American the Meteorological Soc*iety 82:2,217–2,243, http://dx.doi.org/10.1175/1520-0477(2001)082<2217:BTBOBM>2.3.CO;2.

Dee, D.P., S.M. Uppalaa, A.J. Simmonsa, P. Berrisforda, P. Polia, S. Kobayashib, U. Andraec, M.A. Balmasedaa, G. Balsamoa, P. Bauera, and others. 2011. The ERA-Interim reanalysis: Configuration and performance of the data assimilation system. *Quarterly Journal of the Royal Meteorological Society* 137:553–597, http://dx.doi.org/10.1002/qj.828.

Dopplick, T.G. 1979. Radiative heating of the global atmosphere: Corrigendum. *Journal of Atmospheric Sciences* 36:1,812–1,817, http://dx.doi.org/10.1175/1520-0469(1979)036<1812:RHOTGA>2.0.CO;2.

Drazin, P.G., and L.N. Howard. 1966. Hydrodynamic stability of parallel flow of inviscid fluid. Pp 1–89 in *Advances in Applied Mechanics*, vol. 9. Academic Press.

Fairall, C.W., E.F. Bradley, D.P. Rogers, J.B. Edson, and G.S. Young. 1996. Bulk parameterization of air-sea fluxes for Tropical Ocean-Global Atmosphere Coupled-Ocean Atmosphere Response Experiment. *Journal of Geophysical Research* 101(C2):3,747–3,764, http://dx.doi.org/10.1029/95JC03205.

Findlater, J. 1969. A major low-level air current near the Indian Ocean during the northern summer. *Quarterly Journal of the Royal Meteorological Society* 95:362–380, http://dx.doi.org/10.1002/qj.49709540409.

Fischer, A.S., R.A. Weller, D.L. Rudnick, C.C. Eriksen, C.M. Lee, K.H. Brink, C.A. Fox, and R.R. Leben. 2002. Mesoscale eddies, coastal upwelling, and the upper-ocean heat budget in the Arabian Sea. *Deep Sea Research Part II* 49:2,231–2,264, http://dx.doi.org/10.1016/S0967-0645(02)00036-X.

Gadgil, S. 2003. The Indian monsoon and its variability. *Annual Review of Earth and Planetary Sciences* 31:429-467, http://dx.doi.org/10.1146/annurev.earth.31.100901.141251.

Ghosh, S.K. 1978. Influence of the Arabian Sea on the Indian summer monsoon. *Tellus* 30:117–125, http://dx.doi.org/10.1111/j.2153-3490.1978.tb00825.x.

Holtslag, A.A.M., and B.A. Boville. 1993. Local versus nonlocal boundary-layer diffusion in a global climate model. *Journal of Climate* 6:1,825–1,842, http://dx.doi.org/10.1175/1520-0442(1993)006<1825:LVNBLD>2.0.CO;2.

Liu, W.T., K.B. Katsaros, and J.A. Businger. 1979. Bulk parameterization of air-sea exchanges of heat and water vapor including the molecular constraints at the interface. *Journal of Atmospheric Sciences* 36:1,722–1,735, http://dx.doi.org/10.1175/1520-0469(1979)036<1722:BPOASE>2.0.CO;2.

Lock, A.P., A.R. Brown, M.R. Bush, G.M. Martin, and R.N.B. Smith. 2000. A new boundary layer mixing scheme: Part I. Scheme description and single-column model tests. *Monthly Weather Review* 128:3,187–3,199, http://dx.doi.org/10.1175/1520-0493(2000)128<3187:ANBLMS>2.0.CO;2.

Lucas, A., E. Shroyer, H.W. Wijesekera, H.J.S. Fernando, E. D'Asarso, M. Ravichandran, S.U.P. Jinadasa, J.A. MacKinnon, J.D. Nash, R. Sharma, and others. 2014. Mixing to monsoons: Air-sea interactions in the Bay of Bengal. *Eos, Transactions American Geophysical Union* 95(30)269–270, http://dx.doi.org/10.1002/2014EO300001.

McPhaden, M.J., G. Meyers, K. Ando, Y. Masumoto, V.S.N. Murty, M. Ravichandran, F. Syamsudin, J. Vialard, L. Yu, and W. Yu. 2009. RAMA: The Research Moored Array for African-Asian-Australian Monsoon Analysis and Prediction. *Bulletin of the American Meteorological Society* 90:459–480, http://dx.doi.org/10.1175/2008BAMS2608.1.

Miles, J.W. 1986. Richardson's criterion for the stability of stratified shear flow. *Physics of Fluids* 29:3,470–3,471, http://dx.doi.org/10.1063/1.865812.

Miles, J.W., and L.N. Howard. 1964. Note on a heterogeneous shear flow. *Journal of Fluid Mechanics* 20:331–336, http://dx.doi.org/10.1017/S0022112064001252.

Rao, P.S. 2005. Arabian Sea monsoon experiment: An overview. *Mausam* 56:1–6.

Schott, F.A., S.-P. Xie, and J.P. McCreary Jr. 2009. Indian Ocean circulation and climate variability. *Reviews of Geophysics* 47, RG1002, http://dx.doi.org/10.1029/2007RG000245.

Strang, E.J., and H.J.S. Fernando. 2001a. Entrainment and mixing in stratified shear flows. *Journal of Fluid Mechanics* 428:349–386, http://dx.doi.org/10.1017/S0022112000002706.

Strang, E.J., and H.J.S. Fernando. 2001b. Vertical mixing and transports through a stratified shear layer. *Journal of Physical Oceanography* 31:2,026–2,048, http://dx.doi.org/10.1175/1520-0485(2001)031<2026:VMATTA>2.0.CO;2.

Tennekes, H., and A.G.M. Driedonks. 1981. Basic entrainment equations for the atmospheric boundary layer. *Boundary Layer Meteorol*ogy 20:515–531, http://dx.doi.org/10.1007/BF00122299.

Webster, P.J., V.O. Magana, T.N. Palmer, J. Shukla, R.A. Tomas, M. Yanai, and T. Yasunari. 1998. Monsoons: Processes, predictability, and prospects for prediction. *Journal of Geophysical Research* 103(C7):14,451–14,510, http://dx.doi.org/10.1029/97JC02719.

Weller, R.A., M.F. Baumgartner, S.A. Josey, A.S. Fischer, and J.C. Kindle. 1998. Atmospheric forcing in the Arabian Sea during 1994–1995: Observations and comparisons with climatology and models. *Deep Sea Research Part II* 45:1,961–1,999, http://dx.doi.org/10.1016/S0967-0645(98)00060-5.

Wijesekera, H.W., E. Shroyer, A. Tandon, M. Ravichandran, D. Sengupta, P. Jinadasa, H.J.S. Fernando, N. Agrawal, K. Arulananthan, M. Baumgartner, and others. In press. ASIRI: An ocean-atmosphere initiative for Bay of Bengal. *Bulletin of the American Meteorological Society*, http://dx.doi.org/10.1175/BAMS-D-14-00197.1.

Zeng, X., M. Zhao, and R.E. Dickinson. 1998. Intercomparison of bulk aerodynamic algorithms for computation of sea surface fluxes using TOGA COARE and TAO data. *Journal of Climate* 11:2,628–2,644, http://dx.doi.org/10.1175/1520-0442(1998)011<2628:IOBAAF>2.0.CO;2.

AUTHORS

G.S. Bhat (bhat@caos.iisc.ernet.in) is Professor, Centre for Atmospheric and Oceanic Sciences, Indian Institute of Science, Bangalore, India. **Harindra J.S. Fernando** is the Wayne and Diana Murdy Endowed Professor, Department of Civil & Environmental Engineering & Earth Sciences, and Department of Aerospace and Mechanical Engineering, University of Notre Dame, Notre Dame, Indiana, USA.

APPENDIX A. DEPENDENCE OF THE EXCHANGE COEFFICIENTS OF HEAT FLUXES ON WIND SPEED
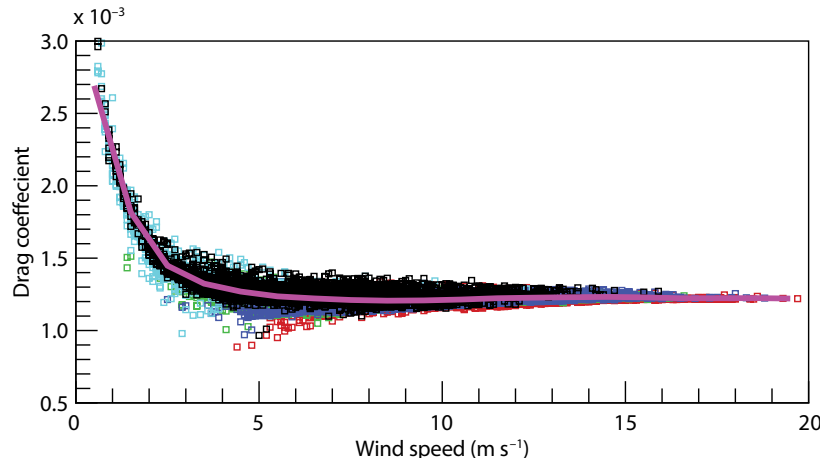
Exchange coefficients for latent heat flux (C_e) and sensible heat flux (C_h) are equal. Individual values of latent and sensible heat fluxes were computed taking 30-minute averaged quantities and using the Zeng et al. (1998) algorithm, which is based on the Monin-Obukhov similarity theory for the atmospheric surface layer. The procedure yields the surface fluxes without employing exchange coefficients. Then the exchange coefficients were derived from the respective bulk formulae (see Equations 2 and 5 in the text). All available data from the Bay of Bengal Monsoon Experiment (e.g., Bhat et al., 2001) and the Arabian Sea Monsoon Experiment (e.g., Rao, 2005) cruises were used. The solid line shows the average value as a function of wind speed, which was used in computing the fluxes shown in Figure 1.

APPENDIX B. ESTIMATION OF HEAT FLUX, Q_T, AT THE TOP OF THE MIXED LAYER

In modeling studies, the driving processes of Q_t are the surface buoyancy flux (B_0), the surface shear stress (τ_0), and the wind shear near the top of the ML (e.g., Tennekes and Driedonks, 1981; Lock et al., 2000). Q_t is parameterized, but it is not unique. One such formulation is (e.g., Lock et al., 2000):

$$Q_t = \rho\, C_p\, w_e\, l\, \partial\theta/\partial z; \qquad Q_t = \rho\, C_p\, K_h\, (Ri_g)\, \partial\theta/\partial z, \qquad (A1)$$
$$\text{(I)} \qquad\qquad\qquad \text{(II)}$$

where w_e is the entrainment velocity, l is an appropriate length scale, and K_h is the eddy thermal diffusivity that depends on Ri_g. The term w_e in (I) is related to surface buoyancy flux and surface shear stress since the turbulence they generate in the ABL entrains higher θ air at the top of the ML. Term (II) arises from local instability of an SSL. Vertical profiles of temperature and wind speed are required for estimating (I) and (II) in Equation A1. To get a feel for the Q_t, we consider one specific example, namely, the formulation for Q_t used in the GFDL coupled climate model (Lock et al., 2000; Anderson et al., 2004) and estimate its predicted Q_t for the ARMEX soundings shown in Figure 6. In the GFDL model, Q_t is calculated by employing (I) and (II), and the maximum between the two is used to force the model. On June 26, the surface layer was nearly neutrally stable, and ABL was turbulent due to strong winds. There were few scattered cumulus clouds. For these conditions, the expression for w_e reduces to $w_e = A_1\, A_2\, u_*^3/(z_{ml}\, \Delta b + A_3\, u_*^2)$ (see Equation 1

of Lock et al., 2000). Here, A_1 (= 0.23), A_2 (= 25), and A_3 (= 8.55) are empirical constants, $\Delta b = g\,(\theta_2 - \theta_{ml})/\theta_{ml}$, is a buoyancy force term, z_{ml} is mixed layer height, and $u_* = \sqrt{\tau_0/\rho}$. Subscripts 2 and ml refer to the ML top inversion layer and the mixed layer (Figure 2), respectively. Calculating u_* using the bulk flux algorithm of Zeng et al. (1998) gives $u_* \sim 0.4$ m s^{-1} and 0.3 m s^{-1} around the radiosonde launch times on June 26 and July 9, respectively. The corresponding Q_t values are 42 W m^{-2} and 14 W m^{-2}, respectively. In the GFDL model, K_h is given by $K_h = l^2\, f(Ri_g)\, S$, where l is a mixing length scale, S is the magnitude of the horizontal wind shear, $f = 1.0/(1 + 40\, Ri_g)$, $l = kz/(1 + kz/\lambda)$, k is the von Karman constant, and λ is assumed to be proportional to the height of the ABL. The estimated values of Q_t from (II) for June 26 and July 9 soundings are 20 W m^{-2} and 1 W m^{-2}, respectively. The required Q_t on June 26 and July 9 estimated from Equation 1 and neglecting horizontal advection are 20 W m^{-2} and 7 W m^{-2}, respectively. The GFDL model takes the higher value between the two calculated from (I) and (II), so those estimated from the former are forcing the model in these cases. In the real atmosphere, turbulence in the ML will enhance SSL instability when $Ri_g < 1$, and entrainment flux given by (I) and (II) could be working simultaneously. Therefore, we need to understand the relative contributions of (I) and (II) in Equation A1 (instead of taking the larger of the two) to correctly represent the mixing at the top of the ML.